

Salicylic Acid-Modified Sm-TiO₂ for Photoluminescence and Photocatalysis under Real Sunlight: Synergistic Effects between Ligand-to-Metal Charge Transfer (LMCT) and Sm³⁺

Original

Salicylic Acid-Modified Sm-TiO₂ for Photoluminescence and Photocatalysis under Real Sunlight: Synergistic Effects between Ligand-to-Metal Charge Transfer (LMCT) and Sm³⁺ Dopant / Lakhdar, Rostom; Freyria, Francesca S.; Mousdis, George A; Bonelli, Barbara; Elghniji, Kais. - In: JOURNAL OF PHYSICAL CHEMISTRY. C. - ISSN 1932-7447. - 128:32(2024), pp. 13445-13457. [10.1021/acs.jpcc.4c03459]

Availability:

This version is available at: 11583/2994341 since: 2024-11-12T13:42:20Z

Publisher:

American Chemical Society

Published

DOI:10.1021/acs.jpcc.4c03459

Terms of use:

This article is made available under terms and conditions as specified in the corresponding bibliographic description in the repository

Publisher copyright

(Article begins on next page)

Salicylic Acid-Modified Sm-TiO₂ for Photoluminescence and Photocatalysis under Real Sunlight: Synergistic Effects between Ligand-to-Metal Charge Transfer (LMCT) and Sm³⁺ Dopant

Rostom Lakhdar, Francesca S. Freyria, George A Mousdis, Barbara Bonelli, and Kais Elghniji*



Cite This: *J. Phys. Chem. C* 2024, 128, 13445–13457



Read Online

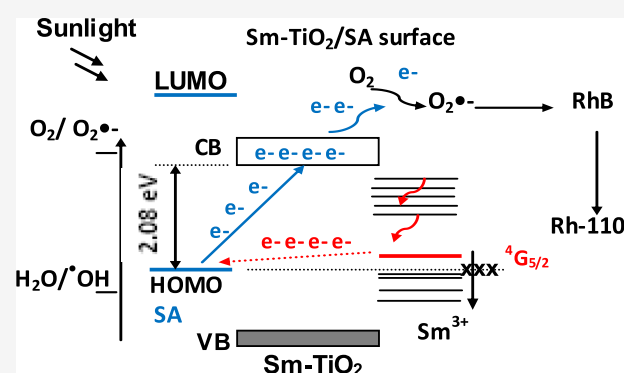
ACCESS |

Metrics & More

Article Recommendations

Supporting Information

ABSTRACT: A salicylic-acid (SA)-modified samarium-doped TiO₂ complex (Sm-TiO₂/SA) was synthesized via a sol-gel method followed by impregnation. A Raman Fourier transform IR and X-ray photoelectron spectroscopic study showed that SA (as an electron donor) forms a surface complex on the Sm-TiO₂ surface through its phenolic/carboxylic functional groups. In the Sm-TiO₂/SA complex, a ligand-to-metal charge transfer (LMCT) is active, inducing a marked red-shift in the absorption spectrum of TiO₂, which extends to 550–600 nm. The synergetic effect between the LMCT process and the luminescent properties of the lanthanide ions (Sm³⁺) is discussed and supported by the photoluminescence spectra. Further photocatalytic experiments (under sunlight) and the study of the effect of different scavengers show the presence of competitive reactions between de-ethylation and cleavage of Rhodamine B (RhB) during its degradation. With the Sm-TiO₂/SA complexes, the superoxide radical ion (O₂^{•−}) is the main active species responsible for the *N*-de-ethylation pathway under sunlight irradiation. The cleavage of RhB by the hydroxyl radical (•OH) appears, instead, to dominate with the Sm-TiO₂ photocatalysts.



1. INTRODUCTION

In recent years, a great deal of effort has been devoted to developing heterogeneous photocatalysts with high sensitivity to the solar radiation spectrum, especially in the visible and near-infrared range. One of the various approaches reported in the literature to deal with this challenge is the surface adsorption of organic molecules onto inorganic semiconductors, such as titanium dioxide (TiO₂). This method may lead to two different sensitization mechanisms. In the former, large dye molecules are adsorbed on the TiO₂ surface, and an electronic transition between the highest occupied molecular orbital (HOMO) and the lowest unoccupied molecular orbital (LUMO) of the dye occurs by absorption of a visible light photon. Such a transition is followed by the injection of the excited free electron from the LUMO of the dye into the conduction band (CB) of TiO₂.^{1–12}

The latter (promising) method to expand the optical response of TiO₂ in the visible region of sunlight is the formation of ligand-to-metal charge transfer (LMCT) complexes on TiO₂. The LMCT method is based on a chemical interaction between small organic molecules [electron-rich ligands such as salicylic acid (SA) or catechol, for instance] and a semiconductor (here, TiO₂). The ligand–TiO₂ complex exhibits a new absorption band with a tail extending to 500–600 nm. In this work, SA was chosen as a ligand that can chemisorb on the TiO₂ particle surface generating a surface complex, such as titanium (IV) salicylate.¹³ In the hybrid interface, an electron-transfer reaction

can occur through an inner-sphere mechanism of the surface complex, with a direct transfer of electrons from the ground state of the organic molecules into the CB of TiO₂ without the involvement of any excited molecular state (HOMO–LUMO) due to the complexation of surface titanium ions. For the sake of convenience, the UV–vis spectra of the TiO₂/SA complex, SA and TiO₂ (anatase) are shown in Figure S1: SA alone has an absorption band centered at ca. 300 nm arising from the transition between its HOMO–LUMO molecular orbitals. For TiO₂, the absorption edge around 400 nm is connected to the intrinsic band gap excitation of anatase. The formation of an LMCT complex between TiO₂ and the SA ligand is accompanied by the appearance of a visible light absorption band, which is not seen with either the SA or TiO₂ alone.

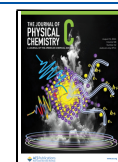
The number of documents on LMCT-mediated visible light photocatalysis is undergoing an exponential increase. The consistent viewpoint confirms that a stable and efficient organic ligand–TiO₂ complex should satisfy the following parameters: (i) the presence of a chemical linkage (i.e., covalent bond)

Received: May 26, 2024

Revised: July 13, 2024

Accepted: July 15, 2024

Published: August 6, 2024



between the adsorbate and the TiO_2 surface (in this case probably a dative covalent bond);^{14,15} (ii) both TiO_2 and the (small) organic adsorbate do not absorb visible light separately, but after their interaction, a surface complex forms, giving rise to visible light-driven LMCT¹⁶ (Figure S1). Taking these factors into consideration, the degradation of organic molecules under visible light powered by surface complex photocatalysis is a formidable challenge.

Very recently, some of us provided strong evidence that the LMCT process could enhance the charge separation efficiency, leading to a higher photocurrent and promising photocatalytic performances of an SA-modified Dy- TiO_2 complex.¹⁷ In that work, our attention focused on the quenching effect induced by LMCT on oxygen defect-related emissions. The relation between the LMCT and the photoluminescence (PL) of the Dy^{3+} dopant was not among the purposes of the previous paper. Stimulated by this previous success, here we want instead to study the synergetic effect between the LMCT process in samarium-doped TiO_2 (Sm-TiO_2) coupled with SA and the luminescent properties of the lanthanide ion Sm^{3+} used for doping as both should markedly influence visible-light-driven photocatalysis.

In this article, we report an assessment of the PL and the photocatalytic properties under real sunlight of a $\text{Sm-TiO}_2/\text{SA}$ LMCT complex. Based on our previous experience, a nonpolar solvent (hexane) was selected to ensure chemical linkage (chelating coordination) between the SA functional groups ($-\text{OH}$ and $-\text{COOH}$ groups) and the $-\text{OH}$ groups at the Sm-TiO_2 surface. The so-obtained $\text{Sm-TiO}_2/\text{SA}$ complex presented strong chemical and thermal stability against decomplexation (vide infra). The Rhodamine B (RhB) dye was used as a model molecule to assess the activity of the Sm-TiO_2 and $\text{Sm-TiO}_2/\text{SA}$ photocatalysts under various light irradiation conditions, including, but not limited to, real sunlight: to support the photocatalytic assessment, other artificial sources in the UV and visible range were employed, and the role of several scavengers has been assessed.

2. MATERIALS AND METHODS

2.1. Preparation of the Sm-TiO_2 and $\text{Sm-TiO}_2/\text{SA}$ Photocatalysts. The undoped and Sm^{3+} -doped TiO_2 photocatalysts were synthesized by the sol-gel method. In a typical preparation, 8.0 mL of tetrabutyl orthotitanate (TBOT, 97%, Merck) was dissolved in 15 mL of absolute ethanol under vigorous stirring for 30 min (solution A). Next, a solution composed of absolute ethanol, acetic acid, and water (volume composition: 7.0, 3.8, and 2.4 mL, respectively) was added dropwise to a flask containing solution A. The mixture was kept under constant stirring for 30 min (solution B). Subsequently, different amounts (0.059, 0.088, and 0.174 g) of samarium (III) chloride (SmCl_3 , 99.9%, Sigma-Aldrich) were dissolved in solution B under continuous stirring, yielding a transparent solution. The nominal Sm/Ti molar percentages in solution B were as follows: 1.0, 1.5, and 3.0%. The obtained transparent sols were kept under constant stirring for 2 h. The transparent gels were left aging for 12 h at room temperature and subsequently dried at 340 K. To remove residual Cl^- ions, the xerogel was adequately washed with deionized water until the pH value was below 7. After washing, the samples were calcined at 748 K for 2 h.

For the preparation of undoped TiO_2 , we followed the same procedure except for the addition of SmCl_3 . The powders will be referred to as undoped TiO_2 and 1% Sm-TiO_2 , 1.5% Sm-TiO_2 ,

and 3% Sm-TiO_2 , respectively, where x % corresponds to the nominal molar Sm/Ti percentage.

The as-prepared powders were impregnated with SA to obtain x % $\text{Sm-TiO}_2/\text{SA}$ powders via impregnation. In a typical impregnation procedure, 25 mg of SA was dissolved in 30 mL of hexane under vigorous stirring at 333 K. After the complete dissolution of SA, the surface modification was carried out by adding 0.2 g of the x % Sm-TiO_2 particles into the SA solutions. The mixtures were kept under continuous stirring in a glovebox until adsorption equilibrium, resulting in a yellow and yellow/brownish color of the powders. After filtration, the x % $\text{Sm-TiO}_2/\text{SA}$ powders were repeatedly washed with distilled water and finally dried at 373 K.

2.2. Characterization Methods. The X-ray diffraction (XRD) patterns were recorded on a Bruker D8 ADVANCE diffractometer. The operating conditions were as follows: $\text{Cu-K}\alpha$ radiation (40 mA, 40 kV, $\lambda = 0.15418$ nm) ranges from 5 to 70° 2θ with a step size of 0.025° and a counting time of 13 s/step.

N_2 adsorption/desorption isotherms at 77 K were obtained on powders that underwent preoutgassing for 4 h to eliminate water and other adventitious contaminants. Two different outgassing temperatures (343 and 423 K) were used based on the presence or absence of SA, respectively, to preserve the organic moiety. The measurements were conducted on a Micromeritics ASAP 2020 Plus instrument (Micromeritics, Norcross, GA, USA). The specific surface area (SSA) and pore size distribution of the samples were determined using the Brunauer-Emmett-Teller method and the Barrett-Joyner-Halenda method on the isotherms' desorption branch, respectively.

The thermogravimetric analysis (TGA) of the samples was carried out on a TGA Q500 in the 303–1023 K temperature range, under dynamic N_2 atmosphere, by putting the powder samples into a Pt crucible, with a heating rate of 283 K min^{−1}.

For field emission scanning electron microscopy (FESEM) micrographs and semiquantitative elemental analysis and elemental maps, a Merlin FESEM instrument (Carl-Zeiss AG, Oberkochen, Germany) equipped with an energy-dispersive X-ray analysis (EDX) probe from Oxford Instruments (Abingdon, UK) was used.

Raman spectra were recorded on a Bruker RFS 100 Raman spectrometer equipped with two laser lines at 514 and 633 nm. The power of the excitation radiation was 150 mW.

Fourier transform IR and attenuated total reflection (FTIR-ATR) spectra were collected in the 4000–500 cm^{−1} region on an FTIR spectrophotometer (Equinox 55, Bruker Optics) equipped with a single reflection diamond ATR accessory (Dura-Samp1IR II by SensIR Technologies). Each reported spectrum represents an average of 100 scans at a resolution of 4 cm^{−1}.

Diffuse reflectance (DR) UV-vis spectra of the powders were recorded on a Cary 5000 UV-vis-NIR spectrophotometer (Varian Instruments, Palo Alto, CA, USA) equipped with a DR sphere.

X-ray photoelectron spectroscopy (XPS) analysis was carried out on a PHI 5000 VersaProbe equipment (Physical Electronics, Feldkirchen, Germany) using monochromatic $\text{Al-K}\alpha$ radiation (1486.6 eV) as the X-ray source and a pass-energy of 187.75 eV. The C 1s spectral line shift of the adventitious carbon at a binding energy (BE) value of 284.8 eV was used for charge referencing XPS spectra.

The amount of SA adsorbed on Sm-TiO₂ was evaluated by measuring the aromatic-H signals by nuclear magnetic resonance (¹H NMR): the Sm-TiO₂/SA complex was dissolved in dimethyl sulfoxide for liquid NMR analysis using a Bruker AV 500 spectrometer at 400 MHz (¹H NMR) at room temperature.

2.3. Rhodamine B Photocatalytic Degradation Tests.

The photocatalytic experiments under natural sunlight were carried out between 11:00 a.m. and 1:00 p.m. during March on the roof of the Department of Chemistry, University of Gafsa–Tunisia (latitude 34°35'29" North and longitude 8°47'03" East). The sunlight irradiation pattern was measured using a pyranometer (Environment S.A, France), capable of measuring sunlight irradiation in the range 950–1000 Wm^{−2} and with a sensitivity of 15 mV/W/m².

100 mL portion of aqueous suspensions (5 mg L^{−1}, 10 μM) of RhB (Sigma-Aldrich) and 50 mg of photocatalyst powder were placed in an open Pyrex vessel. Before irradiation, the suspensions were magnetically stirred for 30 min in the darkness to achieve adsorption–desorption equilibrium conditions. No significant RhB adsorption (1–2.75%) had been observed with all of the photocatalysts, in agreement with the acidic environment of the suspensions, in which both the RhB molecules and the TiO₂ anatase surface are positively charged. The pK_a of RhB is 3.7, which means that it exists in its cationic forms (RhBH⁺ and RhBH₂²⁺) and in the zwitterionic form (RhB[±]) below and above pH 3.7, respectively. The pH values of the aqueous phase in the Sm-TiO₂/RhB and Sm-TiO₂/SA/RhB suspensions were found to be in the pH range 3.3–3.7, at which the surface of TiO₂ was positively charged. In such acidic pH range, the RhB will be in its cationic form (RhBH⁺), and, hence, due to electrostatic repulsive forces between RhBH⁺ species and the positively charged surface of the photocatalysts, the adsorption of the RhB should be negligible, in our experimental conditions.

Another set of photocatalytic experiments was carried out under different artificial illumination conditions: (i) under UV illumination using four lamps with a λ_{max} = 254 nm wavelength (11 W low-pressure mercury lamp, Philips, Holland¹⁸) that were vertically positioned outside the Pyrex vessel; (ii) under blue LED (λ_{max} ~ 460 nm) using four lamps (16 W, Philips, Holland) that were positioned outside the Pyrex vessel. Such LED sources were employed to study the possible advantages of LEDs over more “traditional” light sources including lower energy consumption and longer lifetime.

In each photocatalytic experiment, at given irradiation time intervals, the RhB concentration in the photocatalytic reaction mixture was analyzed by following the intensity of the RhB band at 555 nm on a UV–visible spectrophotometer UVD-2950 (Labomed, Los Angeles, CA).

The effects and contributions of capture hydroxyl radicals (•OH), superoxide radicals (O₂^{•−}), holes (h⁺), and electrons (e[−]) in the titania-mediated photocatalytic process were investigated by considering the presence of scavenger species in photocatalytic systems, such as isopropyl alcohol (IPA, 1.5 × 10^{−3} mol L^{−1}), benzoquinone (BQ, 1.5 × 10^{−3} mol L^{−1}), ethylenediaminetetraacetic acid (EDTA, 4 × 10^{−4} mol L^{−1}), and potassium persulfate (K₂S₂O₈, 5 × 10^{−4} mol L^{−1}) in 5 mg L^{−1} RhB solution containing 0.05 g of photocatalysts.

3. RESULTS AND DISCUSSION

3.1. Structural, Textural, and Morphological Characterization. Figure 1 reports the XRD patterns of the undoped and the doped samples: with all the patterns, only the anatase

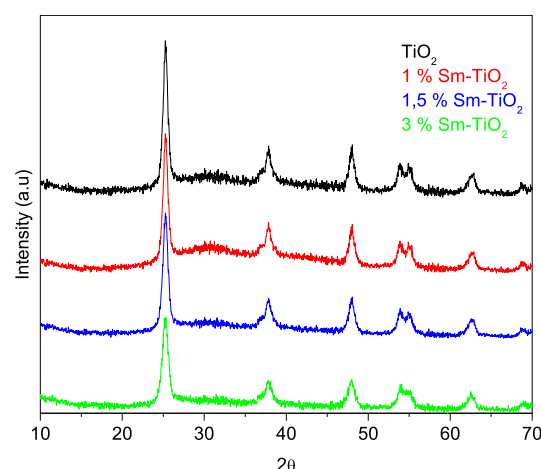


Figure 1. XRD patterns of undoped and Sm-doped TiO₂ samples calcined at 748 K.

phase was detected (in accordance with the JCPDF: 21-1272 file for the anatase crystalline structure of TiO₂).¹⁹ Moreover, all of the samples show a broad signal at around 31.3° 2θ values, probably due to the presence of a small fraction of amorphous TiO₂. The diffraction peaks of Sm₂O₃-like species (expected at 2θ values of 19.88, 28.26, 32.75, 46.99, and 55.74°, JCPDF: 74-1807) could not be identified even in the XRD patterns of 3% Sm-TiO₂ in agreement with their small quantity, below the detection limit of XRD.

The average crystallite size of all samples was calculated via Scherrer's equation using the full-width at half-maximum of six Bragg peaks. The average crystallite size of undoped TiO₂ was determined to be ~13.2 nm, i.e., a higher value than that for the doped ones (Table 1). Since the ionic radius of octahedral Sm³⁺ ions (0.96 Å) is larger than that of octahedral Ti⁴⁺ ions (0.61 Å), the partial insertion of Sm species into the TiO₂ crystal lattice results in an increase in the lattice parameters (and the cell volume) in the doped samples (Table 1).

The different growth of TiO₂ particles with and without Sm-doping was corroborated by the aspect of the gels, namely, translucent with undoped TiO₂ and transparent with Sm-doping (Figure S2). The main reason for this result is that acetic acid in the synthesis mixture (having a CH₃COOH/TBOT ≥ 2) can act as a chelating agent to form less reactive Ti-[(OH)_y(OOCCH₃)_x] species. The acetate Ti complex undergoes slow, controlled hydrolysis and condensation, generating fine spherical primary particles and a translucent viscous TiO₂ gel.^{20,21} Apart from the role of acetic acid in the sol–gel mixture, doping with Sm leads instead to transparent viscous gels: this result confirms that the Sm dopant effectively limits the growth of TiO₂ primary particles (leading to the transparency of the Sm-TiO₂ gels).

N₂ isotherms measured at 77 K are reported in Figure S3 for some selected samples: type IV isotherms are observed, with an H2-type hysteresis loop, typical for mesoporous materials with (likely interparticles) ink-bottle pores. The PSD of the undoped TiO₂ sample, which has an SSA of 32 m²g^{−1}, shows a peak centered at ca. 3.4 nm, with a small tail at ca. 4.5 nm. SA chemisorption on the undoped TiO₂ does not affect the average porous size (ca 3.5 nm) much but improves the homogeneity of the PSD and slightly increases the SSA (51 m²g^{−1}).

Sm doping leads to an increase in both the average pore size (ca 6.7 nm) and the SSA (101 m²g^{−1}). The SSA increase agrees with the hypothesis that dopant Sm³⁺ ions suppress the growth

Table 1. Relevant Structure Parameters as Obtained from the Samples' XRD Patterns and the Corresponding Rietveld Analysis^a

sample	Scherrer's crystallite size (nm)	lattice parameters		
		<i>a</i> (Å)	<i>c</i> (Å)	<i>V</i> (Å ³)
TiO ₂	13.2 (1)	3.78557 (0.00069)	9.50247 (0.00181)	136.175 (0.044)
1% Sm-TiO ₂	12.6 (1)	3.79222 (0.00214)	9.50379 (0.00651)	136.9758 (0.301)
1.5% Sm-TiO ₂	12.8 (1)	3.79648 (0.00157)	9.50964 (0.00440)	137.056 (0.102)
3% Sm-TiO ₂	9.3 (2)	3.79134 (0.00126)	9.51249 (0.00351)	137.742 (0.057)

^aThe value of the *R* profile in all of the refinements was below 12% of the powder sample.

of TiO₂ particles. With Sm-doped TiO₂, the presence of SA slightly decreases the SSA to 76 m²g⁻¹ and shifts the maximum of the PSD to ca. 5.6 nm. As it will be shown by FTIR spectroscopy, the presence of Sm should favor the chemical link of the SA molecules to the Sm-TiO₂ surface, as compared to undoped TiO₂, and this phenomenon, in turn, could induce aggregation of the TiO₂ particles, leading to a decrease of both SSA and (interparticles) pores diameter. This is in good agreement with the TGA results (Figure S4), which show that the decomposition of the SA ligand in the 1.5% Sm-TiO₂/SA complex took place at temperatures as high as 523–723 K. Such chemical stability can be due to covalent interactions (e.g., –COOTi– links), capable of stabilizing the SA ligand and delaying its decomposition.

The morphological characterization of the as-prepared samples (Figure S5) was carried out by a FESEM instrument equipped with an EDX probe that was used to perform elemental analysis and collect elemental maps (Figure S6). The TiO₂ sample shows spherical primary particles undergoing agglomeration/aggregation. Upon Sm doping, the particles still looked uniformly distributed in size. The elemental maps of Ti, O, and Sm were well-defined with a sharp contrast. The profile of Sm was close to that of Ti and O, which indicated that the Sm is evenly distributed throughout the Sm-TiO₂ material (Figure S6).

For the Sm-TiO₂/SA complexes, some aggregation was observed, likely due to the formation of a chemical bond between the SA ligand and the Sm-TiO₂ surface. This explanation has also been proposed in carboxylic acid-modified CuO nanoparticles by Loya et al.²²

Table 2 reports the Sm/Ti molar percentage of a set of selected samples, as determined by both EDX and XPS. It should

Table 2. Sm/Ti Molar Percentage of Some Representative Sm-TiO₂ and Sm-TiO₂/SA Samples, as Determined by EDX (with Standard Deviations in the 1–3–24% Range) and XPS Analyses

sample	EDX-determined Sm/Ti molar %	XPS-determined Sm/Ti molar %
1.5% Sm-TiO ₂	1.1	0.5
1.5% Sm-TiO ₂ /SA	1.0	0.5
3% Sm-TiO ₂	2.1	1.3
3% Sm-TiO ₂ /SA	2.0	0.6

be remarked that the latter technique is more representative of the surface composition of materials, whereas EDX should be able to evaluate also inner atomic layers, though in a semiquantitative way. Considering the limits of both techniques, according to XPS Sm is less abundant at the surface of the NPs, and the effect of the presence of SA molecules on the surface is more evident with the sample at 3% Sm/Ti molar percentage, in

that by XPS a smaller Sm concentration is detected in the 3% Sm-TiO₂/SA complex. As it will be shown by FTIR spectroscopy, probably the surface Sm³⁺ ions act as Lewis sites toward the benzene ring of the SA molecule (acting as a base) and thus a fraction of surface Sm³⁺ is likely “masked” by SA molecules, finally explaining the lower surface Sm/Ti ratio detected by XPS in the 3% Sm-TiO₂/SA sample.

3.2. Raman, IR, XP, and DR-UV–vis Spectroscopic Studies. The vibrational properties of the TiO₂ lattice (Raman scattering and true electronic-vibrational transitions) and the luminescence of the Sm³⁺ dopant (fluorescence, virtual electronic-vibrational transitions) can be assessed separately by comparing the spectra collected with two different laser excitations at λ_{ex} = 633 and 514 nm, respectively.

All the Raman spectra were extracted following the spectral shift (Δω, cm⁻¹) to wavelength (nm) conversion using the following equations²³

$$\Delta\omega = \left(\frac{1}{\lambda_{\text{ex}}} - \frac{1}{\lambda} \right) 10^7 \quad (1)$$

$$\lambda = \frac{1}{\left(\frac{1}{\lambda_{\text{ex}}} - \frac{\Delta\omega}{10^7} \right)} \quad (2)$$

where Δω is the Raman shift (cm⁻¹), λ_{ex} is the laser excitation wavelength (nm), and λ is the peak position (nm).

Under laser excitation at λ_{ex} = 514 nm, both the undoped TiO₂ and Sm-TiO₂ samples show the true Raman bands of TiO₂ anatase phase at 518 nm (Δω ~ 147 cm⁻¹), 525 nm (~401 cm⁻¹), 528 nm (~511 cm⁻¹), and 532 nm (~641 cm⁻¹), in agreement with XRD results.²⁴

Since excitation at 514 nm is close to the ⁶H_{5/2}–(⁴G + ⁴F)_{7/2} absorption transitions of Sm³⁺, the luminescence of Sm³⁺ could be detected in the spectral range of 560–625 nm (~1900–3350 cm⁻¹). Therefore, the Raman bands at 583 nm (~2314 cm⁻¹), 606 nm (~2956 cm⁻¹), 612 nm (~3112 cm⁻¹), and 620 nm (3325 cm⁻¹) are assigned to Sm³⁺-related emissions [⁶H_{5/2}–(⁴G + ⁴F)_{7/2}], and the signal intensities strongly depend on the Sm³⁺ concentration^{25–27} (Figure 2a).

For the Sm-TiO₂/SA samples (Figure 2b), the Sm³⁺-related emissions could hardly be seen in the 537–625 nm range. This phenomenon could be related to the occurrence of an LMCT complex between the SA ligand and the TiO₂ surface, as will be discussed based on PL and UV–vis spectroscopies measurements. However, the Raman spectra display only the vibrational modes of TiO₂ and the SA molecule adsorbed on the Sm-TiO₂ surface^{28,29} (as detailed in Table S1). The two bands of the carboxyl group [δ_(O–H) at 552 nm and ν_(COO–) at 561.6 nm] are substituted by two broad bands centered at 551.9 and 560.7 nm; correspondingly, the phenolic bands (δ_(O–H) at 545 nm and δ_(C–O) at 554 nm) were not observed in the Sm-TiO₂/SA samples. This result confirms that the phenolic (–OH) and

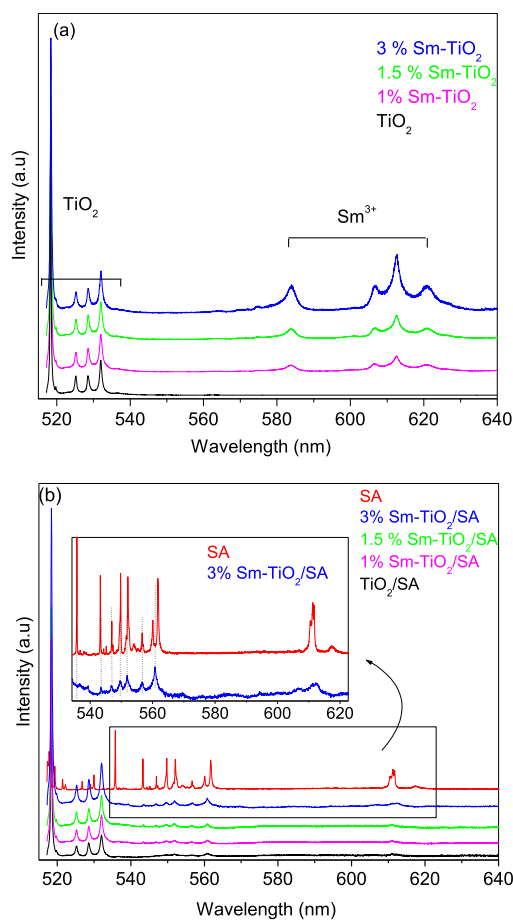


Figure 2. Raman spectra of the undoped TiO₂ and the Sm-TiO₂ samples (a); Raman spectra of SA and its complexes with the undoped TiO₂ and the Sm-TiO₂ samples (b). Insets to section (b) show a magnification of the profiles of the Raman spectra of SA and the 3% Sm-TiO₂/SA complex in the 537–625 nm range.

carboxylic groups (–COOH) of SA are strongly bonded with the Sm-TiO₂ surface.¹³ The benzene ring bands at 535, 538, and 560 nm are also affected by the new environment, as confirmed by the FT-IR analysis reported in the following paragraph.

Under laser excitation at $\lambda_{\text{ex}} = 633$ nm (Figure S7), the Sm-TiO₂ and Sm-TiO₂/SA samples show only the true Raman bands corresponding to vibrational modes of TiO₂ anatase and the SA molecule. The Sm³⁺-related emission cannot be observed on excitation at 633 nm because this wavelength does not match the excited states of Sm³⁺.

Figure 3 depicts the FTIR ATR spectra of undoped TiO₂ and Sm-TiO₂ powders before and after SA modification. For the undoped TiO₂ and the Sm-TiO₂ samples (Figure 3a), the bands at 1634 and 3354 cm^{−1} correspond to the bending and asymmetric stretching vibrational modes of molecular water, respectively: as a whole, the Sm-TiO₂ samples have more surface-adsorbed water and hydroxyl groups than the undoped TiO₂.

The IR spectrum of free SA showed some characteristic vibrational peaks of the aromatic ring and phenolic/carboxylic acid functional linkage groups (i.e., –OH and –COOH). More precisely, the –OH and C–OH phenolic groups (bands at 1240, 1324, and 1187–1248 cm^{−1}), the –OH carboxylic acid (band at 881 cm^{−1}), the C–O carboxylic acid (bands at 1296 and 1379 cm^{−1}), and the C=O carbonyl group (bands at 1581 and 1655–

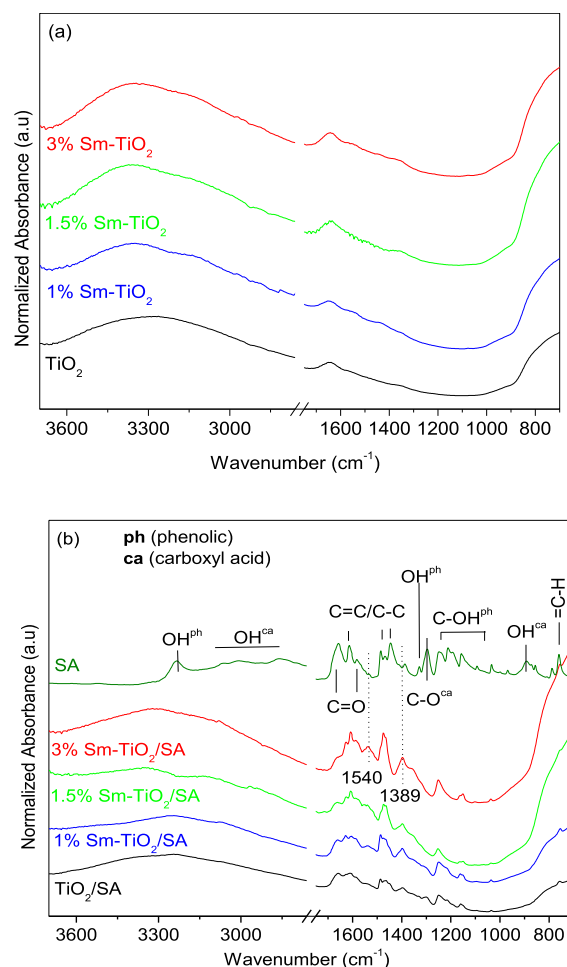


Figure 3. ATR-FTIR spectra (from bottom to top) of the undoped TiO₂, the Sm-TiO₂ samples (a), the Sm-TiO₂/SA complexes, and SA (b).

1680 cm^{−1}) are observed.³⁰ The bands attributed to the benzene aromatic ring bonds of the SA molecule are seen at 1606, 1619, 1471, and 1481 cm^{−1} (aromatic C=C stretching bands); C–C stretching at 1444 cm^{−1} and =C–H bending, at 750 cm^{−1}.

All the SA surface-modified samples show new bands at 1389 and 1540 cm^{−1}, characteristic of symmetric and antisymmetric vibration of COO[−] groups in –COOTi species.³¹ The disappearance of C–OH bands is likely due to the involvement of the phenolic group in the formation of the SA-TiO₂ complex. An important finding from the IR spectra is that the SA benzene ring bands are also affected by the new environment, and the C=C peaks are found at 1468, 1457, and 1606 cm^{−1} (dotted arrows), indicating that changes in electronic distribution are propagated to the whole aromatic ring.^{31–33}

ATR spectroscopy shows that the surface modification of TiO₂ and Sm-TiO₂ samples with SA results in the disappearance of SA functional linkage groups (Figure 3b).³¹ The formation of SA bound to the Sm-TiO₂ surface is confirmed by the ¹H NMR spectrum of a selected 1.5% Sm-TiO₂/SA complex, which shows similar field position and splitting of the aromatic-H signals between 6.5 and 8 ppm as for SA molecules. The broad OH signal at 11–12 ppm disappeared completely, indicating the chemical link of the SA molecules to the Sm-TiO₂ surface (Figure S8). As compared to the TiO₂/SA sample, the Sm-TiO₂/SA samples show an increase of the bands at 1389 and 1540 cm^{−1} (–COOTi group) (solid arrows) with increasing

Sm^{3+} concentration. This means that the Sm^{3+} and Ti^{4+} species are simultaneously involved in the coordination of the SA ligand in the $\text{Sm-TiO}_2/\text{SA}$ complex, leading to chemical stability.³⁴ This result is in good agreement with previous NMR studies,³⁵ reporting that the Sm^{3+} ions may form Lewis acid–base complexes with SA molecules at the surface of the TiO_2 , leading to a higher adsorption capacity compared to undoped TiO_2 .

XPS was employed as an additional tool to investigate the surface chemical states of the as-prepared samples and assess the interaction of SA with Sm-TiO_2 .

The XPS survey spectra of three representative samples, namely, undoped TiO_2 , 1.5% Sm-TiO_2 , and 1.5% $\text{Sm-TiO}_2/\text{SA}$, are shown in Figure S9. The high-resolution (HR) XP spectrum in the range of the Ti 2p lines consists of two peaks at the BE values reported in Figure S10a, readily assigned to the Ti $2p_{3/2}$ and Ti $2p_{1/2}$ lines.³⁶ Such values are consistent with those reported in the literature for the Ti^{4+} species at the surface of anatase TiO_2 . The comparison between the HR Ti 2p spectrum of undoped TiO_2 and 1.5% Sm-TiO_2 indicates that the latter suffers a small BE shift to lower energy. The decrease in BE may be attributed to some local environment changes derived from the introduction of Sm^{3+} .³⁷ However, the observed splitting is ca. 5.8 eV with both undoped TiO_2 and 1.5% Sm-TiO_2 samples, indicating that only the Ti^{4+} species are present. Conversely, after SA modification, the Ti $2p_{3/2}$ peak of the 1.5% $\text{Sm-TiO}_2/\text{SA}$ complex is slightly shifted toward higher energy, and a slightly smaller splitting (ca. 5.7 eV) is observed, along with a small shoulder at ca. 457 eV that can be due to the Ti $2p_{3/2}$ peak of (reduced) Ti^{3+} species, likely stabilized by the interaction with the SA ligand.³⁸ It has to be remarked that the corresponding Ti $2p_{1/2}$ peak is less evident in the curve due to the different intensities of the two lines of Ti.

The presence of the SA ligand coordinated to the 1.5% Sm-TiO_2 surface can be ascertained by observing the HR spectra of the O 1s and C 1s lines. The O 1s HR spectrum shows three peaks located at 529.1, 530.3, and 531.6 eV, corresponding to Ti–O bonds (lattice oxygen) and C=O and –OH groups (Figure S10b), respectively. The O 1s/Ti 2p ratio is around 2.5, i.e., slightly higher than the stoichiometric ratio in TiO_2 , in agreement with the presence of SA at the surface. The HR C 1s spectrum shows four main peaks at 283.37, 284.8, 286.7, and 288.9 eV, which are characteristic of the C–H (aromatic), C–C/C=C (aromatic), C=O, and C–O–Ti/O–C=O groups, respectively.³⁹ No signal that can be ascribed to Ti–C bonds was observed at 281 eV, indicating that the C atoms of the SA ligand did not dope the TiO_2 lattice.

Figure S10c reports the HR Sm 3d XP spectra of the 3% Sm-TiO_2 and 3% $\text{Sm-TiO}_2/\text{SA}$ samples, showing the occurrence of a (small) fraction of surface Sm^{3+} species (line at BE = 1083.42 eV, a value close to the BE of the Sm $3d_{5/2}$ line in Sm_2O_3). Such signals were not clearly detectable with the 1.5% Sm-doped samples, likely due to the very low amount of surface Sm^{3+} species.

The DR UV–vis spectra of the as-prepared samples are shown in Figure 4. For the undoped TiO_2 , the typical absorption edge occurs around 400 nm due to the charge-transfer transition of O^{2-} to Ti^{4+} in anatase.⁴⁰ As compared to the absorption edge of undoped TiO_2 , the absorption edges of the Sm-TiO_2 samples are blue-shifted (Figure 4a, Table 3), showing that the Sm-doped samples mostly absorb in the UV range and should not be able to exploit efficiently the visible fraction of sunlight.^{41,42} As expected, the absorption peaks in the vis–IR spectral region (at 418, 439, 477, 500, 526, 562, 944, 1072, 1227, 1380, 1482,

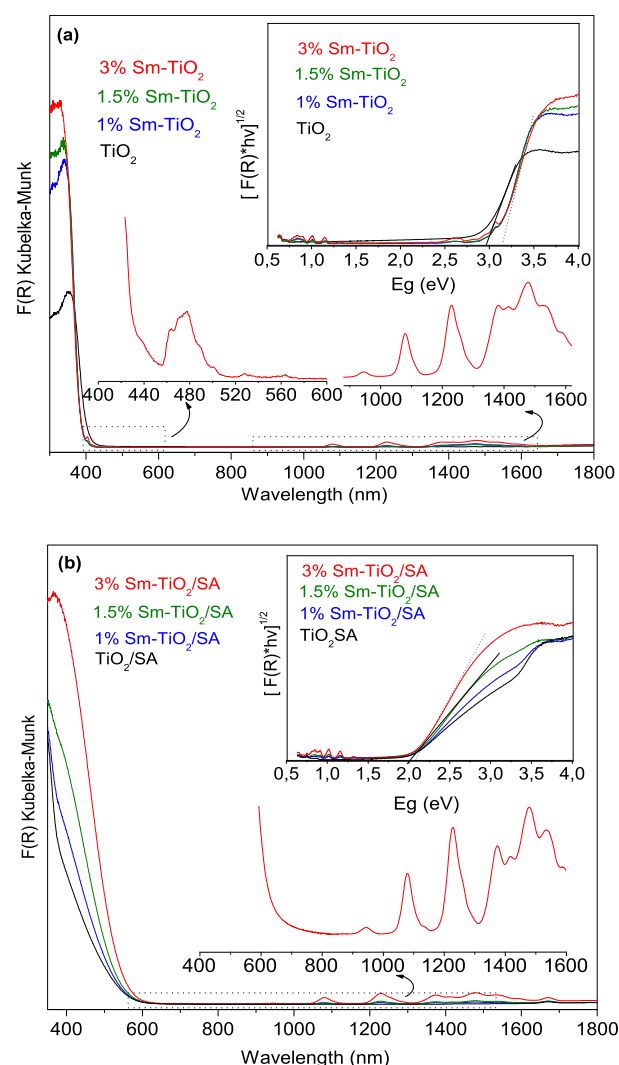


Figure 4. DR-UV–vis spectra of undoped TiO_2 and Sm-TiO_2 samples (a), TiO_2/SA and $\text{Sm-TiO}_2/\text{SA}$ complexes (b). The insets show the corresponding Tauc's plots.

Table 3. Optical Band Gaps of the Undoped TiO_2 , the Sm-TiO_2 Samples, and the SA Complexes

sample	E_g (eV)	sample	E_g (eV)
TiO_2	2.96	TiO_2/SA	2.10
1% Sm-TiO_2	3.10	1% $\text{Sm-TiO}_2/\text{SA}$	2.12
1.5% Sm-TiO_2	3.13	1.5% $\text{Sm-TiO}_2/\text{SA}$	2.11
3% Sm-TiO_2	3.12	3% $\text{Sm-TiO}_2/\text{SA}$	2.03

1530, and 1587 nm) correspond to the f – f transitions from $^6\text{H}_{5/2}$ ground state to $^6\text{P}_{5/2}$, $^4\text{G}_{9/2}$, $^4\text{M}_{15/2}$, $^4\text{G}_{7/2}$, $^4\text{F}_{5/2}$, $^4\text{G}_{5/2}$, $^6\text{F}_{11/2}$ et $^6\text{F}_{9/2}$ and $^6\text{F}_{7/2}$, $^6\text{F}_{5/2}$, $^6\text{F}_{3/2}$, $^6\text{H}_{15/2}$, and $^6\text{F}_{1/2}$ excited states of Sm^{3+} species.⁴³

Interestingly, the SA complexation red-shifts the absorption onset of the Sm-TiO_2 samples up to 550–600 nm (Figure 4b). This phenomenon was followed by a color change of the Sm-TiO_2 powders from white to yellow upon SA complexation (not shown). The extension of the $\text{Sm-TiO}_2/\text{SA}$ absorption in the visible region suggests a broad distribution of surface electronic states, possibly related to a variety of SA ligand– Ti^{4+} charge-transfer (LMCT) complexes. The LMCT mechanism promotes electron-transfer efficiency to the CB of TiO_2 , extending the

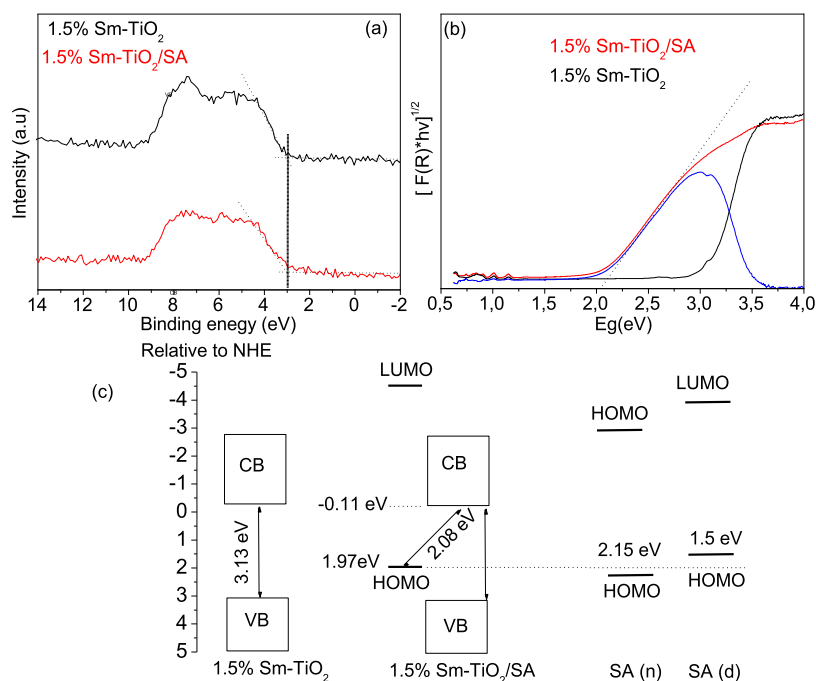


Figure 5. XPS-determined valence band spectra of the 1.5% Sm-TiO₂ and 1.5% Sm-TiO₂/SA samples (a). Differential Tauc plot (blue) between 1.5% Sm-TiO₂ and 1.5% Sm-TiO₂/SA (b). Diagram of energy with respect to potential versus the normal hydrogen electrode (c). Position of HOMO of SA in both neutral (n) and deprotonated (d) forms, as previously established in ref 47.

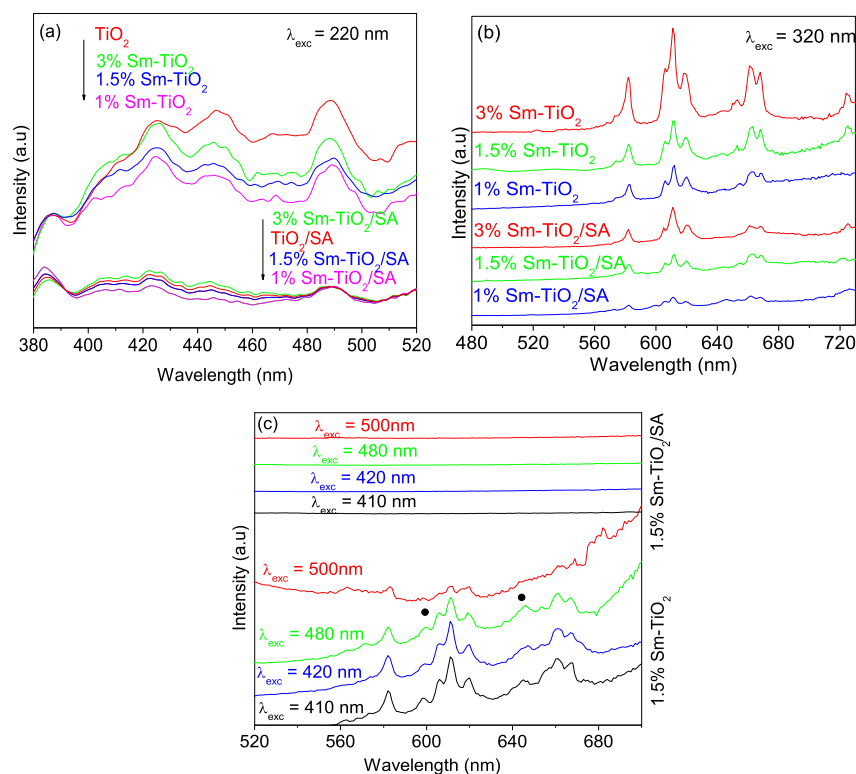


Figure 6. Emission spectra of the Sm-TiO₂ and Sm-TiO₂/SA samples excited at 220 (a) and 320 nm (b). Emission spectra of 1.5% Sm-TiO₂ and Sm-TiO₂/SA samples excited at 410, 420, 480, and 500 nm (c).

absorption threshold toward the visible region.⁴⁴ It is noteworthy that the f–f absorptions of Sm³⁺ ions at 401–562 nm overlapped with the absorption red-shift. A comparative discussion with the literature is difficult here, since, to the best of our knowledge, there are no relevant bibliographic data on this subject.

The band gap energy (E_g) values in Table 3 were obtained by extrapolating the linear region of the Tauc's plot $[(F(R) \cdot h\nu)^{1/2} \text{ vs } (h\nu)]$, as obtained by considering indirect semiconductors, with anatase being the main phase. In agreement with the blue-shift observed in the DR UV–vis spectra, the band gap energy increases with Sm-doping up to 1.5% Sm, then no significant

change is observed at higher Sm levels, as likely some surface Sm species forms at 3% Sm (as observed by XPS analysis). Instead, the decrease of band gap energies observed in the presence of SA is attributed to the LMCT from the HOMO of the SA ligand to the CB of TiO₂ and the formation of Ti–O–C covalent bond, which is supported by both IR and XPS evidence.

The position of the valence band maximum (VBM) of Sm-TiO₂ and Sm-TiO₂/SA was determined by XPS through linear extrapolation of the onset of their VB emission: the VBM of 1.5% Sm-TiO₂ and 1.5% Sm-TiO₂/SA were located at +3.018 eV (Figure 5a). Considering the *E_g* values determined by Tauc's plot, the position of the corresponding CB minima (CBM) would occur at −0.11 eV. Figure 5b shows the differential Tauc's plot between 1.5% Sm-TiO₂ and the 1.5% Sm-TiO₂/SA samples. The new plot (blue curve) gives an intercept at an energy of 2.08 eV, satisfactorily matching the Tauc's plot-determined *E_g* value (~2.11 eV) of 1.5% Sm-TiO₂/SA. It can be ascribed to the energy difference between HOMO of SA (~1.97 eV) and CBM edge of Sm-TiO₂ (−0.11 eV).^{8,45,46} The HOMO state of 1.5% Sm-TiO₂/SA is in good agreement with those reported for SA adsorbed on TiO₂ through the chelating configuration.⁴⁷ Because of the LMCT between the SA ligand and Sm-TiO₂, the alignment of the bands at the hybrid interface is staggered, as shown by the energy diagram of 1.5% Sm-TiO₂/SA (Figure 5c).

3.3. Photoluminescence Emission Spectroscopy

Study. Figure 6 shows the PL emission spectra of Sm-TiO₂ and Sm-TiO₂/SA samples under various excitation wavelengths at 220, 320, and 410–500 nm. These bands are observed in the PL excitation spectra of the as-prepared samples (Figure S11). The excitation band at 220 nm is attributed to TiO₂ host lattice absorption. The band at 320 nm lies above the TiO₂ band gap and coincides with the f–f transition ⁶H_{5/2}–⁴P_{3/2} of Sm³⁺ ions. The excitations bands in the visible range (410, 420, 480, and 500 nm) correspond to f–f transition from ground state ⁶H_{5/2} to the ⁴G_{7/2}, ⁴D_{7/2}, ⁴D_{3/2} and ⁴M_{15/2} excited states of Sm³⁺ ions.⁴⁸

Under excitation at 220 nm (Figure 6a), the PL spectra show corresponding PL emissions of excitons, such as photoinduced electrons trapped by some surface oxygen vacancies (OVs) and defects, as well as the recombination of photoinduced electrons and holes.^{49,50} All of the samples exhibit PL signals with comparable curve shapes, which confirm the presence of defects in the host lattice. The PL peak intensity of 1% Sm-TiO₂ is lower than that of 1.5% Sm-TiO₂ and 3% Sm-TiO₂, which indicates that an excessive amount of Sm has a detrimental effect on the recombination of photogenerated electrons and holes.

Upon SA surface modification, the PL emissions from the surface states and defects are quenched. The PL quenching may have originated from contributions from the presence of the SA ligand as an electron trap center. The combination of the SA ligand and Sm-TiO₂ led to the quenching of luminescence probably due to the increased electron shuttling from the TiO₂ CB and defect states to the ligand through the LMCT process in the Sm-TiO₂/SA complex.³⁹ A similar PL quenching was also observed in the LMCT complexes on TiO₂ using various electron-rich ligands (glucose, catechol, and carboxylate-rich porous carbon, xanthene, and ascorbic acid).^{39,51,52}

When the Sm-TiO₂ samples are excited at 320 nm (Figure 6b), the PL spectra showed emission lines at around 584, 612, 664, and 726 nm that can be referred to as the ⁴G_{5/2} → ⁶H_{5/2}, ⁶H_{7/2}, ⁶H_{9/2}, and ⁶H_{11/2} direct intra f–f transitions of Sm³⁺ ions, respectively.^{53,54} We believe that all these transitions are associated with the intra-f–f emission of Sm³⁺ ions. The sharp

emission lines indicate that Sm³⁺ ions were mainly incorporated within the TiO₂ matrix in an ordered environment. This agrees with Raman scattering data about the anatase structure of the Sm-TiO₂ samples.

The PL emission intensity at 612 nm increases with the increase in the Sm³⁺ concentration (3%). This indicates that Sm³⁺ ions are the main emitters at excitation of 320 nm. However, for the Sm-TiO₂/SA samples, a partially quenching phenomenon can be observed at increasing Sm³⁺ concentration with a decrease in the intra-f–f emission of Sm³⁺.

The PL emissions of the 1.5% Sm-TiO₂ and 1.5% Sm-TiO₂/SA samples were also studied under visible excitation wavelengths (λ_{exc} = 410, 420, 480, and 500 nm); these excitation energies almost coincide with excited levels of Sm³⁺ ions (Figure S11). In the case of 1.5% Sm-TiO₂, the emission lines at around 584, 612, 664, and 726 nm can be ascribed to intra f–f transitions of Sm³⁺ ions, as mentioned above.

However, some additional broad emission lines (marked with circle symbols) were clearly detectable under direct excitation λ_{exc} = 480 nm (not observable under 320 nm excitation) (Figure S12). This suggests that two types of Sm³⁺-related emission centers may occur in anatase TiO₂. The existence of several Sm³⁺ emission centers points out the presence of charged defects (probably OVs) in the proximity of Sm³⁺ ions.²⁷

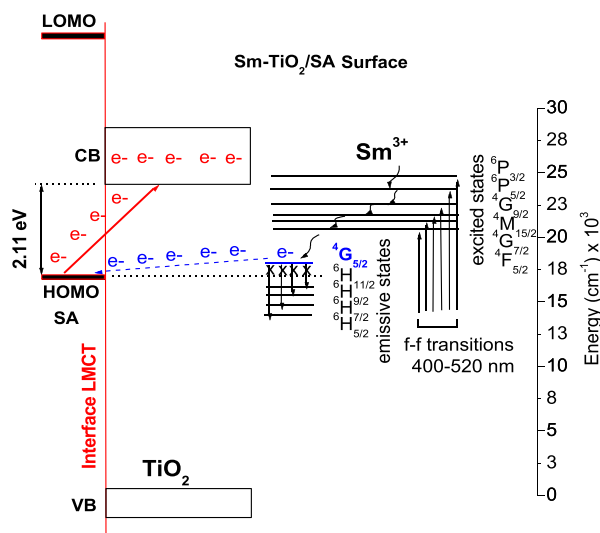
In contrast, all the Sm-TiO₂/SA complexes (as shown here for 1.5% Sm-TiO₂/SA) did not show any emission peak (Figure 6c), suggesting that the intra-f–f transitions of Sm³⁺ are strongly suppressed.

A possible reason for the disappearance of PL emissions of Sm³⁺ ions after SA modification is that the energy level of the LMCT states of Sm-TiO₂/SA samples (~587–610 nm, 17,035–16,430 cm^{−1}) lie below the energy state of ⁴G_{5/2} (~562 nm, 17,980 cm^{−1}). Thus, nonresonant energy transfer is possible implying the energy released through emissive state ⁴G_{5/2} to SA ligand HOMO state, resulting in the quenching of Sm³⁺-related emission centers (Scheme 1). The DR spectra of Sm-TiO₂/SA samples show that the absorption onset overlaps with the f–f transitions of Sm³⁺ (~400–562 nm). This phenomenon was also reported by Li et al.,⁵⁵ who investigated the energy-transfer mechanism and PL properties of lanthanide-containing polyoxotitanate cages coordinated by salicylate ligands [LnTi₆O₃(OiPr)₉(salicylate)₆]. They argued that the LMCT state of salicylate-Ti⁴⁺ is too low in energy to facilitate energy transfer to Ln³⁺ (Tb³⁺ and Dy³⁺), resulting in the absence of Tb³⁺ and Dy³⁺ emission signals. When the complexes Sm-TiO₂/SA absorb photons of visible light, the electrons are transferred from the SA ligand HOMO state to the TiO₂ CB and then migrate to the surface (to initiate photocatalytic reactions).

A practical way to confirm the above results is to evaluate the intensity of intra-f–f transitions (emission) of Sm³⁺ ions after removing the SA ligand. Figure 7 shows the emission spectra of 3% Sm-TiO₂/SA obtained after heat treatments at 423, 523, and 723 K. As can be verified, the PL emission of Sm-TiO₂/SA cannot be observed after treatments at 423 and 523 K due to the thermal and chemical stability of the SA ligand.⁵⁶ With an increase in the heat treatment temperature to 723 K, emission lines similar to that of Sm-TiO₂ were observed, indicating the removal of the SA ligand. Here, the emissions of Sm³⁺ ions within the Sm-TiO₂/SA complex are mainly governed by the LMCT process between the SA ligand and the Sm-TiO₂ surface.

3.4. Photocatalytic Activity of the Sm-TiO₂ and Sm-TiO₂/SA Samples. 3.4.1. Photodegradation of RhB under Various Light Irradiation Sources. Figure 8a shows the

Scheme 1. LMCT Process and Transitions between the SA Ligand and the CB of Sm-TiO₂ (Red Bold-Arrow)^a



“The 2.11 eV gap corresponds exactly to the energy difference (cm^{-1}) between the HOMO of SA and the CBM of TiO_2 (see Table 2). Non-resonant energy transfer is possible implying the energy releasing through emissive state $^4\text{G}_{5/2}$ to SA ligand HOMO state (blue dash-arrow).”

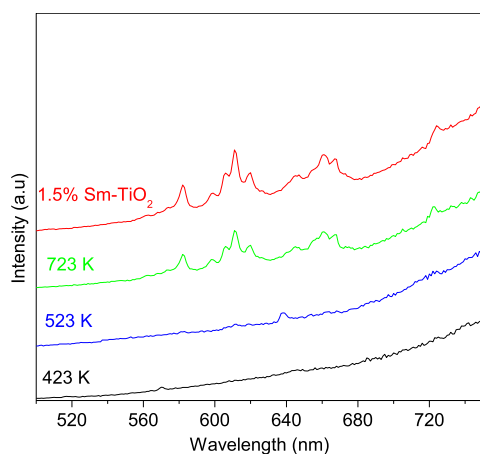


Figure 7. PL emission spectra of 3% Sm-TiO₂/SA treated at various calcination temperatures.

dependence of the photodegradation of RhB on the Sm^{3+} concentration under natural sunlight irradiation. As already detailed in the experimental section (*vide supra*), RhB adsorption is very unlikely in the adopted experimental conditions, in which both the molecule and the photocatalysts' surface are positively charged. A blank experiment made in the absence of any photocatalyst shows that the degradation of RhB due to mere photolysis could be negligible, being much lower ($\sim 4.0\%$) than that due to photocatalysis (black symbols).

The order of removal efficiency of RhB with the different photocatalysts under sunlight in the adopted experimental conditions was as follows: 1% Sm-TiO₂ (99.2%) > 1.5% Sm-TiO₂ (86.7%) > 3% Sm-TiO₂ (81.4%) > undoped TiO₂ (34.3%)

The different photocatalytic activity observed under sunlight irradiation can be explained considering the emission properties of Sm^{3+} ions: the PL emissions show that the Sm^{3+} ion is the main efficient emitter under UV ($\lambda_{\text{exc}} = 320 \text{ nm}$) and visible

excitations ($\lambda_{\text{exc}} = 410\text{--}500\text{ nm}$). In this contest, the PL emission process competes with the RhB photodegradation reaction, thus lowering the photocatalytic activity of the Sm-TiO₂ samples, and, especially at Sm³⁺ doping larger than 1.0%, the photoemission process is more efficient. This competition was also reported in the literature for Eu³⁺-doped oleate-capped TiO₂ NCs.⁵⁷

The PL spectra ($\lambda_{\text{exc}} = 220 \text{ nm}$) show that the intensity of the Sm-TiO₂ samples' spectra was lower than that of undoped TiO₂, demonstrating that the separation of photogenerated carriers was promoted. This was attributed to the introduction of Sm in TiO₂ to generate defects (OVs, Ti³⁺) (as shown for 1.5% Sm-TiO₂/SA) capturing photoinduced electrons, which could effectively enhance the photocatalytic activity of the Sm-TiO₂ photocatalysts.

Therefore, based on these results, the 1% Sm-TiO₂ sample was selected to proceed with the next photocatalytic experiments.

The corresponding apparent reaction constants (k) were quantitatively estimated by applying a pseudo-first-order model [$\ln(C_0/C) = kt$] for RhB degradation (Figure S13a,b). Obviously, the degradation rate of RhB within 120 min over 1% Sm-TiO₂ under sunlight irradiation was found 1.14 and 1.25 folds higher than that of 1.5% Sm-TiO₂ and 3% Sm-TiO₂, respectively.

Figure 8b shows the absorbance changes at 555 nm of RhB on 1% Sm-TiO₂ photocatalyst under sunlight and UV light (Figure S14a): the characteristic absorption band of the RhB molecule around 555 nm decreased gradually, and a very limited shift of the maximum absorbance of RhB was observed at the end of the photocatalytic process (120 min). This result indicates that the cleavage of the conjugated chromophore structure is the main RhB degradation pathway with the 1% Sm-TiO₂ sample.

The enhancement of the photocatalytic activity of Sm-TiO₂ photocatalysts under UV and sunlight irradiation can be attributed to the following factors: (i) doping of Sm³⁺ causes a blue-shift of the absorption edge in the UV range. Hence, the prepared Sm-TiO₂ samples can utilize the UV light fraction of sunlight with more efficiency than undoped TiO₂; (ii) the dispersion of Sm³⁺ ions on the TiO₂ surface/grain boundaries can lead to a charge imbalance, which is likely compensated by hydroxyl groups. Thus, the addition of Sm³⁺ ions can lead to an enhancement of the surface concentration of hydroxyl groups, in agreement with the FTIR ATR spectroscopy results shown in Figure 3. The extrahydroxyl groups could react with the photogenerated holes (h⁺) to form very active hydroxyl radicals (•OH), increasing the photocatalytic efficiency. According to the literature, the •OH species predominantly attack the chromophore structure and induce the cleavage of the ring structure of the RhB molecule.⁵⁸

The photocatalytic properties of the SA-modified Sm-TiO₂ samples improved significantly under sunlight irradiation (Figure 8c). The order of removal efficiency of RhB with the different photocatalysts was 1% Sm-TiO₂/SA (99.8%) \triangleq 1.5% Sm-TiO₂/SA > 3% Sm-TiO₂/SA > TiO₂/SA within 60 min. This is consistent with the DR-UV-vis spectra, which indicate a broader red-shift of the absorption for 1% Sm-TiO₂/SA compared to 1% Sm-TiO₂ samples. Therefore, significantly enhanced photocatalytic activity was achieved under sunlight and blue LED irradiation.

The apparent rate constants of 1% Sm-TiO₂/SA, 1.5% Sm-TiO₂/SA, 3% Sm-TiO₂/SA, and TiO₂/SA are 0.074 \pm , 0.070, 0.034, and 0.0085 min⁻¹, respectively (Figure S13c,d).

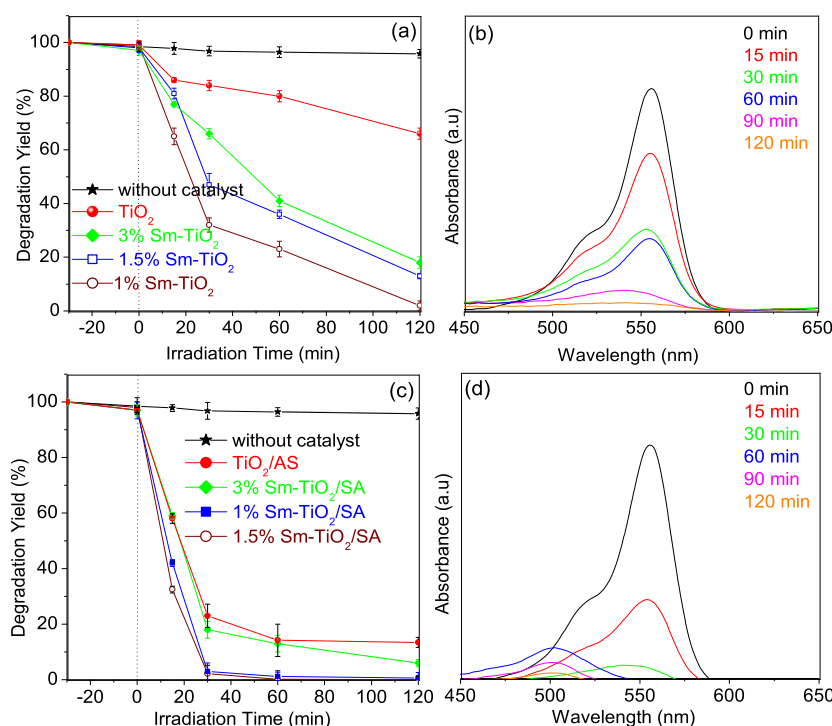


Figure 8. Degradation of RhB with TiO_2 and Sm-TiO_2 samples under sunlight irradiation (a). Normalized UV–vis spectra during the degradation of RhB for 1.0% Sm-TiO_2 under sunlight (b). Degradation of RhB with the TiO_2/SA and $\text{Sm-TiO}_2/\text{SA}$ samples under sunlight irradiation (c). Normalized UV–vis spectra during the degradation of RhB for the 1.0% $\text{Sm-TiO}_2/\text{SA}$ under sunlight (d).

Comparison of the C/C_0 shows that the 1% $\text{Sm-TiO}_2/\text{SA}$ needs only 60 min to achieve 100% removal of RhB, i.e., 60 min in advance as compared to the 1% Sm-TiO_2 sample.

Figure 8d shows the intensity change of the RhB absorbance band at 555 nm of RhB with the 1% $\text{Sm-TiO}_2/\text{SA}$ photocatalyst under sunlight. Under both sunlight and blue light (Figure S14b), the main absorption band of RhB (at 555 nm) decreases rapidly in the first 30 min owing to the cleavage of the RhB aromatic ring. However, after 60 min of the photocatalytic process irradiation, the shift of wavelength reaches a maximum at 497 nm. This new peak position resulted from the *N*-de-ethylated product (namely, rhodamine, Rh-110).^{59,60} At this stage, the color of the dispersion changed from an initial pink to a light brown-yellow color. The absorption intensity at 555 nm declines continuously, but the peak position is no longer shifting, which indicates that both *N*-de-ethylation and cleavage of the aromatic ring occur simultaneously, but *N*-de-ethylation is predominant during the early stage of illumination, according to the literature.⁶¹

3.4.2. Identification of the Photocatalytically Active Species by In Situ Capture Experiments. Radical trapping experiments were carried out to investigate the role of reactive species in the photocatalytic degradation of RhB with 1% Sm-TiO_2 and 1% $\text{Sm-TiO}_2/\text{SA}$ under sunlight irradiation (Figures S15 and S16).

For the 1% Sm-TiO_2 sample (Figure S15), the addition of IPA and EDTA induced a significant decrease in the degradation efficiency, indicating that the $\bullet\text{OH}$ radicals and photogenerated holes h^+ are the main initiative species in the degradation of RhB through the cleavage of the chromophore structure.

When $\text{K}_2\text{S}_2\text{O}_8$ was added to the 1% $\text{Sm-TiO}_2/\text{RhB}$ system, the degradation of RhB was enhanced, and 95% of RhB was removed in 30 min of the photocatalytic process. $\text{S}_2\text{O}_8^{2-}$ ions are capable of scavenging the photogenerated electron e_{CB}^- , thus

increasing the concentration of h_{VB}^+ , with a subsequent higher $\bullet\text{OH}$ concentration on the TiO_2 surface. $\text{S}_2\text{O}_8^{2-}$ ions can also lead to the generation of additional $\bullet\text{OH}$ radicals, as well as sulfate ($\text{SO}_4^{\bullet-}$) radicals in solution. The promotion of the charge separation followed by an increased production of $\bullet\text{OH}$ and the generation of additional $\bullet\text{OH}$ and $\text{SO}_4^{\bullet-}$ radicals could explain the enhancing effect of $\text{S}_2\text{O}_8^{2-}$. Moreover, 85% of RhB was degraded after 120 min when BQ was added into the system, indicating that the $\text{O}_2^{\bullet-}$ species were not responsible for the degradation in the 1.0% Sm-TiO_2 system under sunlight irradiation.

In the case of 1% $\text{Sm-TiO}_2/\text{SA}$, the addition of IPA results in the decreased intensity of the RhB band at 555 nm with a limited blue-shift (Figure S16), similar to what was observed when RhB was degraded in the absence of scavengers. This result indicates that the free $\bullet\text{OH}$ radicals do not participate in the *N*-de-ethylation of RhB. Since the standard redox potential of $\text{H}_2\text{O}/\bullet\text{OH} \sim 2.7$ eV is lower than the HOMO state of SA, the $\bullet\text{OH}$ radical was not efficiently generated by the LMCT SA system under sunlight irradiation.⁶² The absorbance of RhB was reduced remarkably when EDTA was added, suggesting that the holes can directly oxidize RhB. When BQ was added to the reaction system, the RhB degradation was inhibited, and the *N*-de-ethylation process was not observed. Adding $\text{K}_2\text{S}_2\text{O}_8$ gives similar behavior to BQ due to the absence of $\text{O}_2^{\bullet-}$ species. This result is consistent with the findings reported by Huang et al.,⁶³ who reported that $\text{O}_2^{\bullet-}$ species had strong advantages in attacking the *N*-ethyl group, leading to Rh-110 rather than the cleavage of the RhB-conjugated structure.

4. CONCLUSIONS

A stable and novel visible-light-sensitive $\text{Sm-TiO}_2/\text{SA}$ complex was synthesized via a sol–gel procedure followed by

impregnation. FESEM analysis confirmed that the Sm-TiO₂ samples consist of spherical primary particles and that the morphology was maintained after impregnation with SA.

The IR and XP spectroscopic studies of the Sm-TiO₂/SA complex highlight the presence of the aromatic ring and phenolic and carboxylic acid functional groups of the SA ligand. In the presence of Sm species, the interaction of SA with the surface is enhanced, likely due to the formation of Lewis acid/base adducts.

DR UV-vis spectroscopy indicates that the LMCT mechanism induces visible light absorption in both the TiO₂/SA and Sm-TiO₂/SA samples. With increasing concentration of Sm³⁺, the absorption edge increases from 584 to 610 nm, indicating that Sm³⁺ ions are involved in the LMCT mechanism, which was supported by the PL analysis, showing that Sm³⁺ ions efficiently emit under both UV ($\lambda_{\text{exc}} = 320$ nm) and visible sources ($\lambda_{\text{exc}} = 410$ –500 nm).

Due to the limited contribution of Sm³⁺ PL, the 1% Sm-TiO₂ and 1% Sm-TiO₂/SA samples exhibited higher photocatalytic activity, in terms of RhB total conversion, than the other doped samples and of undoped TiO₂ under sunlight irradiation. The reasons are, however, different and related to the optical properties of the two samples: 1% Sm-TiO₂ can efficiently exploit the UV fraction of sunlight, whereas the 1% Sm-TiO₂/SA complex can efficiently exploit the visible fraction of sunlight.

The cleavage of the conjugated chromophore structure is the main RhB degradation pathway with the Sm-TiO₂ samples. The synergistic effect of both the LMCT process and the Sm³⁺ doping leads to selective photocatalytic conversion (*N*-de-ethylation) of RhB to Rh-110 with the Sm-TiO₂/SA samples. The different pathways could be due to the different active species ($\bullet\text{OH}$ and $\bullet\text{O}_2^-$) generation mechanisms occurring in these two materials.

■ ASSOCIATED CONTENT

SI Supporting Information

The Supporting Information is available free of charge at <https://pubs.acs.org/doi/10.1021/acs.jpcc.4c03459>.

UV-vis spectra of Sm-TiO₂ and the TiO₂/SA complex; appearance characters of TiO₂ gels; N₂ adsorption-desorption isotherms and PSD curves; TGA curves of samples, FESEM images, EDX maps, and spectra of all samples; vibrational frequencies of the 1.5% Sm-TiO₂/SA complex; Raman spectra of 1.5% Sm-TiO₂ and 1.5% Sm-TiO₂/SA samples with 633 nm laser excitation; ¹H NMR spectra of SA and the 1.5% Sm-TiO₂/SA complex; XPS survey spectra of all samples; XPS analyses (HR) of Sm-TiO₂ and Sm-TiO₂/SA samples; PL excitation and emission spectra of the 1.5% Sm-TiO₂ and 1.5% Sm-TiO₂/SA samples; degradation of RhB and the first kinetic curves of all samples; UV-vis spectra of RhB for the 1.0% Sm-TiO₂ (UV light) and 1.0% Sm-TiO₂/SA (blue LED); and UV-vis spectra of degraded RhB in the presence of scavengers: IPA, EDTA, K₂S₂O₈, and BQ (PDF)

■ AUTHOR INFORMATION

Corresponding Author

Kais Elghniji — Laboratory of Materials Applications in Environment, Water and Energy LAMEEE (LAM3E), Faculty of Sciences of Gafsa, University of Gafsa, Gafsa 2112, Tunisia;

orcid.org/0000-0001-7367-3095; Email: k.elghniji@yahoo.fr

Authors

Rostom Lakhdar — Laboratory of Materials Applications in Environment, Water and Energy LAMEEE (LAM3E), Faculty of Sciences of Gafsa, University of Gafsa, Gafsa 2112, Tunisia

Francesca S. Freyria — Department of Applied Science and Technology and INSTM-Unit of Torino Politecnico, Torino I-10129, Italy

George A Mousdis — Theoretical and Physical Chemistry Institute, National Hellenic Research Foundation, Athens 11635, Greece; orcid.org/0000-0002-0560-4829

Barbara Bonelli — Department of Applied Science and Technology and INSTM-Unit of Torino Politecnico, Torino I-10129, Italy; Interdepartmental Centre PolitoBIOMed Lab, Torino I-10129, Italy; orcid.org/0000-0002-4716-864X

Complete contact information is available at:

<https://pubs.acs.org/doi/10.1021/acs.jpcc.4c03459>

Notes

The authors declare no competing financial interest.

■ ACKNOWLEDGMENTS

The authors greatly acknowledge the financial support of the Ministry of Higher Education and Scientific Research of Tunisia. This publication is part of the project NODES which has received funding from the MUR—M4C2 1.5 of PNRR funded by the European Union—Next Generation EU (grant agreement no. ECS00000036).

■ REFERENCES

- (1) Luciani, G.; Imparato, C.; Vitiello, G. Photosensitive hybrid nanostructured materials: The big challenges for sunlight capture. *Catalysts* **2020**, *10*, 103.
- (2) Kim, G.; Lee, S. H.; Choi, W. Glucose-TiO₂ charge transfer complex-mediated photocatalysis under visible light. *Appl. Catal., B* **2015**, *162*, 463–469.
- (3) Chen, X.; Peng, X.; Jiang, L.; Yuan, X.; Zhang, J.; Yu, H. Terephthalate acid decorated TiO₂ for visible light driven photocatalysis mediated via ligand-to-metal charge transfer (LMCT). *Colloids Surf., A* **2020**, *603*, 125188.
- (4) Zhang, L.; Yang, J.; Zhao, X.; Xiao, X.; Sun, F.; Zuoa, X. J. N.; Nan, J. Small-molecule surface-modified bismuth-based semiconductors as a new class of visible-light-driven photocatalytic materials: Structure-dependent photocatalytic properties and photosensitization mechanism. *Chem. Eng. J.* **2020**, *380*, 122546.
- (5) Liu, Y.; Mao, J.; Huang, Y.; Qian, Q.; Luo, Y.; Xue, H.; Yang, S. Pt-chitosan-TiO₂ for efficient photocatalytic hydrogen evolution via ligand-to-metal charge transfer mechanism under visible light. *Molecules* **2022**, *27*, 4673.
- (6) Rochkind, M.; Pasternak, S.; Paz, Y. Using dyes for evaluating photocatalytic properties: A critical review. *Molecules* **2015**, *20*, 88–110.
- (7) Kim, M. S.; Yoo, H. Y.; Choi, G. E.; Jo, S.; Shin, H.; Lim, J. Visible light photocatalysis of TiO₂ complexed with albumin via a ligand-to-metal charge transfer (LMCT) pathway. *J. Phys. Chem. C* **2023**, *127*, 5408–5415.
- (8) Imparato, C.; D'Errico, G.; Macyk, W.; Kobielski, M.; Vitiello, G.; Aronne, A. Interfacial charge transfer complexes in TiO₂-enediol hybrids synthesized by sol-sel. *Langmuir* **2022**, *38*, 1821–1832.
- (9) Hovancová, J.; Šišoláková, I.; Vanýsek, P.; Oriňáková, R.; Shepa, I.; Kaňuchová, M.; Király, N.; Vojtko, M.; Cudek, P.; Oriňák, A. Ligand-to-metal charge transfer (LMCT) complex: New approach to non-enzymatic glucose sensors based on TiO₂. *J. Electroanal. Chem.* **2020**, *878*, 114589.

- (10) Peng, T.; Xu, J. An efficient visible-light-responsive surface charge transfer complex AA-TiO₂ based dye-sensitized solar cell. *Optik* **2020**, *207*, 164407.
- (11) Park, H.; Kim, H.; Moon, G.; Choi, W. Photoinduced charge transfer processes in solar photocatalysis based on modified TiO₂. *Energy Environ. Sci.* **2016**, *9*, 411–433.
- (12) Naniwa, S.; Hishitani, S.; Yamamoto, A.; Yoshida, H. Ligand-to-metal charge transfer of a pyridine surface complex on TiO₂ for selective dehydrogenative cross-coupling with benzene. *Phys. Chem. Chem. Phys.* **2021**, *23*, 11366–11373.
- (13) Regazzoni, E. A.; Mandelbaum, P.; Matsuyoshi, M.; Schiller, S.; Bilmes, S. A.; Blesa, M. A. Adsorption and photooxidation of salicylic acid on titanium dioxide: A surface complexation description. *Langmuir* **1998**, *14*, 868–874.
- (14) Kim, G.; Choi, W. Charge-transfer surface complex of EDTA-TiO₂ and its effect on photocatalysis under visible light. *Appl. Catal., B* **2010**, *100*, 77–83.
- (15) Almeida, L. A.; Habran, M.; dos Santos Carvalho, R.; Maia da Costa, M. E. H.; Cremona, M.; Silva, B. C.; Krambrock, K.; Ginoble Pandoli, O.; Morgado, E., Jr.; Marinkovic, B. A. The influence of calcination temperature on photocatalytic activity of TiO₂-acetylacetone charge transfer complex towards degradation of NO_x under visible light. *Catalysts* **2020**, *10*, 1463.
- (16) Zhang, G.; Kim, G.; Choi, W. Visible light driven photocatalysis mediated via ligand-to-metal charge transfer (LMCT): An alternative Approach to solar activation of Titania. *Energy Environ. Sci.* **2014**, *7*, 954–966.
- (17) Ouled Amor, C.; Elghniji, K.; Elaloui, E. Improving charge separation, photocurrent and photocatalytic activities of Dy-doped TiO₂ by surface modification with salicylic acid. *J. Mater. Sci.: Mater. Electron.* **2020**, *31*, 20919–20931.
- (18) Elghniji, K.; Zougari Elwedi, B.; Elaloui, E.; Moussaoui, Y. Photodegradation of 2-chlorophenol in TiO₂/UV system: Phytotoxicity assessment of treated solutions against seedling growth of turnip and tomato. *J. Water Chem. Technol.* **2018**, *40*, 359–366.
- (19) Amor, C. O.; Elghniji, K.; Virlan, C.; Pui, A.; Elaloui, E. Effect of dysprosium ion (Dy³⁺) Doping on morphological, crystal growth and optical properties of TiO₂ particles and thin films. *Phys. B* **2019**, *560*, 67–74.
- (20) Jraba, A.; Anna, Z.; Elaloui, E. Physicochemical properties of La³⁺-doped TiO₂ monolith prepared by sol-gel approach: application to adsorption and solar photodegradation of ibuprofen. *J. Mater. Sci.: Mater. Electron.* **2020**, *31*, 1072–1083.
- (21) Elghniji, K.; Rabah, Z.-A.; Elaloui, E. Novel and facile synthesis of transparent-monolithic TiO₂ gels by sol-gel method based on an esterification reaction. *Mater. Sci. Polym.* **2016**, *34*, 633–640.
- (22) Loya, A.; Stair, J. L.; Uddin, F.; Ren, G. Molecular dynamics simulation on surface modification of quantum scaled CuO nanoclusters to support their experimental studies. *Sci. Rep.* **2022**, *12*, 16657.
- (23) Thyr, J.; Edvinsson, T. Evading the illusions: Identification of false peaks in micro-Raman spectroscopy and guidelines for scientific best practice. *Angew Chem Int Ed Engl.* **2023**, *62*, No. e202219047.
- (24) Pascariu, P.; Cojocar, C.; Airinei, A.; Olaru, N.; Rosca, I.; Koudoumas, E.; Petruta Suche, M. Innovative Ag-TiO₂ nanofibers with excellent photocatalytic and antibacterial actions. *Catalysts* **2021**, *11*, 1234.
- (25) Tiseanu, C.; Cojocar, B.; Parvulescu, V. I.; Sanchez-Dominguez, M.; Primus, P. A.; Boutonnet, M. Order and disorder effects in nano-ZrO₂ investigated by micro-Raman and spectrally and temporarily resolved photoluminescence. *Phys. Chem. Chem. Phys.* **2012**, *14*, 12970–12981.
- (26) Tiseanu, C.; Cojocar, B.; Avram, D.; Parvulescu, V. I.; Vela-Gonzalez, A. V.; Sanchez-Dominguez, M. Isolated centres versus defect associates in Sm³⁺-doped CeO₂: a spectroscopic investigation. *J. Phys. D: Appl. Phys.* **2013**, *46*, 275302.
- (27) Kiisk, V.; Savel, M.; Reedo, V.; Lukner, A.; Sildos, I. Anatase-to-rutile phase transition of samarium-doped TiO₂ powder detected via the luminescence of Sm³⁺. *Phys. Procedia.* **2009**, *2*, 527–538.
- (28) Grabusove, S. A.; Ramanavicius, S.; Popov, A.; Šablinskas, V.; Gogotsi, O.; Ramanavicius, A. Selective enhancement of SERS spectral bands of salicylic acid adsorbate on 2DTi3C2Tx-based MXene film. *Chemosensors* **2021**, *9*, 223.
- (29) Elbagerma, M. A.; Edwards, H. G. M.; Munshi, T.; Hargreaves, M. D.; Matousek, P.; Scowen, I. J. Characterization of New Cocystals by Raman Spectroscopy, Powder X-ray Diffraction, Differential Scanning Calorimetry, and Transmission Raman Spectroscopy. *Cryst. Growth Des.* **2010**, *10*, 2360–2371.
- (30) Li, X.; Xu, H.; Shi, J.-L.; Hao, H.; Yuan, H.; Lang, X. Salicylic acid complexed with TiO₂ for visible light-driven selective oxidation of amines into imines with air. *Appl. Catal., B* **2019**, *244*, 758–766.
- (31) Elghniji, K.; Elaloui, E.; Moussaoui, Y. Coating of anatase titania on clinoptilolite by metal organic chemical vapor deposition method: enhanced mesoporosity and photocatalytic activity. *Chem. Pap.* **2018**, *72*, 1159–1168.
- (32) Ai, C.; Wu, X.; Ke, Y.; Lei, Y.; Shao, X. Synthesis and photocatalytic sterilization performance of SA/TiO₂. *J. Inorg. Organomet. Polym. Mater.* **2020**, *30*, 3378–3387.
- (33) Tunesi, S.; Anderson, M. A. Surface effects in photochemistry: An in situ cylindrical internal Reflection-Fourier Transform Infrared investigation of the effect of ring substituents on chemisorption onto TiO₂ ceramic membranes. *Langmuir* **1992**, *8*, 487–495.
- (34) Jiang, H.; Yan, P.; Wang, Q.; Zang, S.; Li, J.; Wang, Q. High-performance Yb, N,P-tridoped anatase-TiO₂ nano-photocatalyst with Visible light response by sol-solvothermal method. *Chem. Eng. J.* **2013**, *215–216*, 348–357.
- (35) Lakhdar, R.; Ouled Amor, C.; Ben Mosbah, M.; Pui, A.; Moussaoui, Y.; Ben Salem, R.; Elghniji, K. An investigation of the role of samarium on the sol stability, particle growth, optical, and photocatalytic performance of TiO₂. *J. Mater. Sci.: Mater. Electron.* **2023**, *34*, 1043.
- (36) Li, X.; Zheng, H.; Wang, Y.; Li, X.; Liu, J.; Yan, K.; Wang, J.; Zhu, K. Synergistic effect of Y doping and reduction of TiO₂ on the improvement of photocatalytic performance. *Nanomaterials* **2023**, *13*, 2266.
- (37) Yurtsever, H.; Çiftçioğlu, M. The effect of rare earth element doping on the microstructural Evolution of sol-gel titania powders. *J. Alloys Compd.* **2017**, *695*, 1336–1353.
- (38) Macyk, W.; Szaciłowski, K.; Stochel, G.; Buchalska, M.; Kunciewicz, J.; Łabuz, P. Titanium(IV) complexes as direct TiO₂ photosensitizers. *Coord. Chem. Rev.* **2010**, *254*, 2687–2701.
- (39) Bafaqeer, A.; Amin, N. A. S.; Tahir, M.; Ummer, A. C.; Thabit, H. A.; Theravalappil, R.; Usman, J.; Ahmad, N. Construction of glucose precursor carbon/TiO₂ heterojunction with high ligand-to-metal charge transfer (LMCT) for visible light driven CO₂ reduction. *Chem. Eng. Res. Des.* **2024**, *201*, 353–361.
- (40) Kumar Singh, M.; Mehata, M. S. Temperature-dependent photoluminescence and decay times of different phases of grown TiO₂ nanoparticles: Carrier dynamics and trap states. *Ceram. Int.* **2021**, *47*, 32534–32544.
- (41) Khade, G. V.; Suwarnkar, M. B.; Gavade, N. L.; Garadkar, K. M. Sol-gel microwave assisted synthesis of Sm-doped TiO₂ nanoparticles and their photocatalytic activity for the degradation of Methyl Orange under sunlight. *J. Mater. Sci.: Mater. Electron.* **2016**, *27*, 6425–6432.
- (42) Zhu, X.; Zhou, Q.; Xia, Y.; Wang, J.; Chen, H.; Xu, Q.; Liu, J.; Feng, W.; Chen, S. Preparation and characterization of Cu-doped TiO₂ nanomaterials with anatase/rutile/brookite triphasic structure and their photocatalytic activity. *J. Mater. Sci.: Mater. Electron.* **2021**, *32*, 21511–21524.
- (43) Marzouk, S. Y.; Hammad, A. H. Influence of samarium ions on the structural, and optical properties of unconventional bismuth glass analyzed using the Judd-Ofelt theory. *J. Lumin.* **2021**, *231*, 117772.
- (44) Li, M.; Li, Y.; Zhao, J.; Li, M.; Wu, Y.; Na, P. Alizarin-TiO₂ LMCT complex with oxygen vacancies: An efficient visible light photocatalyst for Cr(VI) reduction. *Chin. J. Chem.* **2020**, *38*, 1332–1338.
- (45) Bledowski, M.; Wang, L.; Ramakrishnan, A.; Khavryuchenko, O. V.; Khavryuchenko, V. D.; Ricci, P. C.; Strunk, J.; Cremer, T.; Kolbeck,

C.; Beranek, R. Visible-light photocurrent response of TiO₂-polyheptazine hybrids: Evidence for interfacial charge-transfer absorption. *Phys. Chem. Chem. Phys.* **2011**, *13*, 21511–21519.

(46) Sannino, F.; Pernice, P.; Imparato, C.; Aronne, A.; D'Errico, G.; Minieri, L.; Perfetti, M.; Pirozzi, D. Hybrid TiO₂-Acetylacetonate amorphous gel-derived material with stably adsorbed superoxide radical active in oxidative degradation of organic pollutants. *RSC Adv.* **2015**, *5*, 93831–93839.

(47) Oprea, I. C.; Panait, P.; Gîrțu, M. A. DFT study of binding and electron transfer from colorless aromatic pollutants to a TiO₂ nanocluster: Application to photocatalytic degradation under visible light irradiation. *Beilstein J. Nanotechnol.* **2014**, *5*, 1016–1030.

(48) Chapura, O. M.; Mikhnev, L. V.; Bondarenko, E. A.; Skomorokhov, A. A.; Goncharov, R. A.; Tsagikyan, A. A. Study intra-4f transitions of Sm³⁺ ions under direct photoexcitation in TiO₂. *IOP Conf. Ser.: Mater. Sci. Eng.* **2019**, *597*, 012052.

(49) Lettieri, S.; Pavone, M.; Fioravanti, A.; Amato, L. S.; Maddalena, P. Charge carrier processes and optical properties in TiO₂ and TiO₂-based heterojunction photocatalysts: A Review. *Materials* **2021**, *14*, 1645.

(50) Ramakrishna, G.; Ghosh, H. N. Emission from the charge transfer state of Xanthene dye-Sensitized TiO₂ nanoparticles: A new approach to determining back electron transfer rate and verifying the Marcus inverted regime. *J. Phys. Chem. B* **2001**, *105*, 7000–7008.

(51) Qu, L.; Huang, D.; Shi, H.; Gu, M.; Li, J.; Dong, F.; Luo, Z. TiO₂/carboxylate-rich porous carbon: A highly efficient visible-light-driven photocatalyst based on the ligand-to-metal charge transfer (LMCT) process. *J. Phys. Chem. Solids* **2015**, *85*, 173–179.

(52) D'Amato, C. A.; Giovannetti, R.; Zannotti, M.; Rommozzi, E.; Minicucci, M.; Gunnella, R.; Di Cicco, A. Band gap implications on nano-TiO₂ surface modification with ascorbic acid for visible light-active polypropylene coated photocatalyst. *Nanomaterials* **2018**, *8*, 599.

(53) Katta, V. S.; Chappidi, V. R.; Kumar, A.; Asthana, S.; Raavi, S. S. K. Enriched visible light absorption by Au-embedded Sm³⁺ doped TiO₂ compact photoanode for enhanced dye-sensitized solar cell performance. *Physica B* **2023**, *652*, 414621.

(54) Chang, M.; Song, Y.; Chen, J.; Zhang, X.; Meng, D.; Zhu, H.; Shi, Z.; Zou, H.; Sheng, Y. Multisite luminescence and photocatalytic properties of TiO₂:Sm³⁺ and TiO₂:Sm³⁺@TiO₂/TiO₂:Sm³⁺@SiO₂ luminescent enhancement materials. *J. Alloys Compd.* **2017**, *725*, 724–738.

(55) Li, N.; Subramanian, G. S.; Matthews, P. D.; Xiao, J.; Chellappan, V.; Rosser, T. E.; Reisner, E.; Luo, H. K.; Wright, D. S. Energy transfer and photoluminescence properties of lanthanide-containing polyoxotitanate cages coordinated by salicylate ligands. *Dalton Trans.* **2018**, *47*, 5679–5686.

(56) Sboui, M.; Nsib, M. F.; Rayes, A.; Ochiai, T.; Houas, A. Application of solar light for photocatalytic degradation of Congo red by a floating salicylic acid-modified TiO₂/palmtrunk photocatalyst. *C. R. Chim.* **2017**, *20*, 181–189.

(57) Caschera, D.; Federici, F.; de Caro, T.; Cortese, B.; Calandra, P.; Mezzi, A.; Nigro, R. L.; Toro, R. G. Fabrication of Eu-TiO₂ NCs functionalized cotton textile as a multifunctional photocatalyst for dye pollutants degradation. *Appl. Surf. Sci.* **2018**, *427*, 81–91.

(58) Golubovskaya, A. G.; Kharlamova, T. S.; Gavrilenko, E. A.; Fakhrutdinova, E. D.; Vodyankina, O. V.; Kulinich, S. A.; Svetlichnyi, V. A. Photocatalytic decomposition of Rhodamine band selective oxidation of 5-Hydroxymethylfurfural by β -Bi₂O₃/Bi₁₂SiO₂₀ nanocomposites produced by laser. *J. Compos. Sci.* **2024**, *8*, 42.

(59) Fan, Y.; Chen, G.; Li, D.; Luo, Y.; Lock, N.; Jensen, A. P.; Mamakhel, A.; Mi, J.; Iversen, S. B.; Meng, Q.; et al. Highly selective deethylation of Rhodamine B on TiO₂ prepared in supercritical fluids. *Int. J. Photoenergy* **2012**, *2012*, 173865.

(60) Li, F.; Lu, C.; Xu, B.; Cheng, L.-Y. Photocatalytic degradation of Rhodamine B under visible light irradiation by TiO₂ doped layered zirconium phosphates. *Nanosci. Nanotechnol.* **2020**, *20*, 1697–1703.

(61) Yao, C.; Wang, X.; Zhao, W.; Li, T.; He, Y.; Ran, X.; Guo, L. Probing the facet-dependent intermediate in the visible-light

degradation of RhB by carbon-coated anatase TiO₂ nanoparticles. *J. Alloys Compd.* **2020**, *846*, 156335.

(62) Almeida, L. A.; Dosen, A.; Viol, J.; Marinkovic, B. A. TiO₂-acetylacetone as an efficient source of superoxide radicals under reduced power visible light: photocatalytic degradation of chlorophenol and tetracycline. *Catalysts* **2022**, *12*, 116.

(63) Huang, J.; Nie, G.; Ding, Y. Metal free enhanced photocatalytic activation of dioxygen by g-C₃N₄ doped with abundant oxygen-containing functional groups for selective N-Deethylation of Rhodamine B. *Catalysts* **2020**, *10*, 6.